

## Fe K $\alpha$ line profile in AGNs: average shape and redshift dependence \*

Wei-Ming Mao<sup>1,2,3</sup>, Chen Hu<sup>2</sup>, Jian-Min Wang<sup>2</sup>, Gang Zhao<sup>1</sup> and Shu Zhang<sup>2</sup>

<sup>1</sup> Key Laboratory of Optical Astronomy, National Astronomical Observatories, Chinese Academy of Sciences, Beijing 100012, China; [gzhao@bao.ac.cn](mailto:gzhao@bao.ac.cn), [wangjm@ihep.ac.cn](mailto:wangjm@ihep.ac.cn)

<sup>2</sup> Key Laboratory for Particle Astrophysics, Institute of High Energy Physics, Chinese Academy of Sciences, Beijing 100049, China;

<sup>3</sup> Graduate University of Chinese Academy of Sciences, Beijing 100049, China;

Received 2009 December 16; accepted 2010 May 18

**Abstract** We collect a sample of 381 (271 type I) active galactic nuclei (AGNs) with *XMM-Newton* observations for an analysis of the dependence of Fe K $\alpha$  profiles on redshifts to test the potential cosmological evolution of spins of supermassive black holes (SMBHs). The sample spans a redshift range of  $z = 0.0008 - 4.76$ , which allows us to rebin the sample into 7 redshift groups. Phenomenological analysis of the Fe profile suggested that the line width ( $\sigma$ ) of the narrow or broad Fe line does not show significant changes in redshift range  $z < 0.3$ . Using a physical model, we significantly detect a narrow Fe K $\alpha$  line at 6.4 keV with an average equivalent width (EW) = 160 eV except for the two largest redshift bins. The EW of the Fe line does not show significant changes. We also find a relativistic broad line in three redshift bins ( $z < 0.116$ ,  $0.056 < z < 0.12$  and  $0.12 < z < 0.3$ ) with an average EW = 522 eV.

**Key words:** galaxies: active — X-rays: general — methods: data analysis

### 1 INTRODUCTION

The Fe K $\alpha$  line, as the most prominent feature in the 6–7 keV band<sup>1</sup> in the X-ray spectrum, provides an important diagnostic of the nature of the disk and the central black hole. The line is produced from X-ray irradiation of cold gas around the black hole. If the line comes from the inner part of the accretion disk, which is close enough to the SMBH, it shows a broad and asymmetric relativistic profile due to a series of special and general relativistic effects such as Doppler shift and gravitational redshift. If the line comes from the outer part of the accretion disk or the dust torus which is far from the SMBH, it shows a narrow profile due to less relativistic effects. Thus, a very broad Fe K $\alpha$  emission line is regarded as a powerful probe to test the gravity of the central black hole in AGNs (Fabian et al. 1989), such as in MCG–6–30–15 (Tanaka et al. 1995; Fabian et al. 2002). General relativistic effects become more significant if the SMBH is spinning fast, where the innermost stable circular orbit becomes smaller (Laor 1991). Detailed analysis of the Fe K $\alpha$  line profile provides key information on the spin of the black hole, which is very useful for understanding the accretion and evolution of SMBHs.

---

\* Supported by the National Natural Science Foundation of China.

<sup>1</sup> Line energy depends on the ionization state. The neutral or low-ionization Fe K $\alpha$  line is at 6.4 keV.

**Table 1** Summary of the Fe  $K\alpha$  Line Properties

Ref.	Sources	Redshift	Sample and observations	Broad Fe line	$\sigma - z$	EW $-z$
S05	104 (53 type 1)	<4.5	<i>XMM</i> , the Lockman Hole	yes	...	...
C08	606 (606 type 1)	<3.5	<i>XMM</i> , the <i>AXIS</i> and <i>XWAS</i> <sup>a</sup>	no	...	...
B05	352	0.5–4.0	CDF-N/S <sup>b</sup>	yes	...	no
This work	381 (271 type 1)	<4.8	2XMMi <sup>c</sup>	yes	no	no

Notes: *a*: *XMM-Newton* International Survey (*AXIS*), *XMM-Newton*-2dF wide angle survey (*XWAS*). *b*: *Chandra* Deep Field-North and South (CDF-N/S). *c*: 2XMMi is the incremental second catalog of serendipitous X-ray sources from the *XMM-Newton*. The symbol ... means that this issue is not mentioned in the paper.

References: S05: Streblyanska et al. (2005); C08: Corral et al. (2008); B05: Brusa et al. (2005).

Although many studies have been done, the properties and the origin of the Fe lines are still controversial, even the question of whether the broad component of Fe  $K\alpha$  is truly common. Early results from *ASCA* observations suggested that broad relativistic lines might be common (Nandra et al. 1997), while recent studies of *XMM-Newton* and *Chandra* observations have shown a smaller fraction of sources with broad lines, although a relatively narrow component is observed frequently (Page et al. 2004; Yaqoob & Padmanabhan 2004). However, this disagreement may arise from the different modelings in literatures (Nandra et al. 2007). In order to properly measure the line properties, we need to accurately model the continuum below the line. For the distant faint objects, the counts collected are not enough to model the continuum due to the limitation of observational instruments. Improving the signal to noise ratio by averaging as many spectra together as possible is a solution. Three independent studies have been conducted by Streblyanska et al. (2005), Brusa et al. (2005) and Corral et al. (2008) by stacking the observed spectra to examine if there is a cosmological evolution of the Fe  $K\alpha$  profiles (a brief summary is given in Table 1). Definitely, this has a very strong impact on understanding the cosmological evolution of SMBHs (Wang et al. 2009).

In this paper, we select AGNs from the *XMM-Newton* archive to study the properties of the Fe  $K\alpha$  profile for an examination of the potential evolution of SMBH spins over cosmic time.

## 2 XMM-NEWTON OBSERVATIONS

### 2.1 The Sample

We selected the objects from the target objects of the Incremental Second *XMM-Newton* Serendipitous Source Catalog (2XMMi, Incremental Update of the Second Version). The target observations include 918 observations of about 600 AGNs. We examine the X-ray source counts after data reduction and exclude those objects with EPIC-pn counts less than 100 in the energy band 2–10 keV in order to preserve a minimum spectral quality of the sample. For those sources with multiple observations, we only use the observation which has the largest source counts. Finally, a sample consisting of 381 AGNs is provided and their redshifts can be derived from the NASA/IPAC Extragalactic Database (NED)<sup>2</sup>.

### 2.2 Data Reduction

Only EPIC-pn data were used in our analysis since the effective area of EPIC-pn is much larger than that of EPIC-MOS. All datasets were publicly available. The EPIC-pn raw observation data files (ODFs) were reduced with the *XMM* Science Analysis System (SAS version 6.5) using the standard processing tasks and the latest calibration files. Periods of high background were excluded. We extracted images with photon energies in the range of 0.3–10 keV, and only used events with FLAG = 0 and PATTERN  $\leq$  4. The source spectra were extracted from a circular area centered at

<sup>2</sup> <http://nedwww.ipac.caltech.edu/>

**Table 2** Redshift Bins

Redshift bins	Number of sources	Redshift bins	Number of sources
<0.016	72 (30 type 1)	0.12–0.3	51 (48 type 1)
0.016–0.03	65 (34 type 1)	0.3–2.0	50 (43 type 1)
0.03–0.056	60 (43 type 1)	2.0–4.8	32 (27 type 1)
0.056–0.12	51 (46 type 1)		
0.12–0.3	51 (48 type 1)		

the peak of the source counts with a radius of  $38''$ . The background spectra were extracted from an off-source region with the same radius. We also obtained response matrices using the SAS tasks **rmfgen** and **arfgen**.

### 3 RESULTS AND DISCUSSION

The 381 AGNs were divided into seven groups as shown in Table 2. The criterion for the redshift bins is that the numbers of AGNs are approximately equal in each bin.

#### 3.1 Averaging Method

There are two different methods to average spectra. 1) All individual observed event files are summed together in one merged event file, from which the average spectra are obtained (e.g. Brusa et al. 2005); 2) An individual intrinsic spectrum is deduced from each event file, then the spectra are averaged (e.g. Corral et al. 2008). Here, we apply the method of Corral et al. (2008).

Spectral fits were performed with the XSPEC (version 12.4) software package (Arnaud 1996) to unfold the observed spectra for each source. After being extracted from the event files, the observed spectra were rebinned to ensure that each energy bin has at least 20 counts in order to apply a  $\chi^2$  minimization technique. The spectra of most objects show several different components as follows: soft excess emission, a line like emission feature around 6.4 keV (at the source rest frame), and a power-law continuum. So, we fitted the observed spectra at 0.3–10 keV (excluding the portion of the spectra where the Fe line is present) using a power law model corrected by Galactic absorption and sometimes intrinsic absorption. If necessary, we added a blackbody component to the power law model to present the ‘soft excess.’ For those objects with absorption features due to the warm absorber, we multiplied one or more absorption edges to the above model. Thus, the “best-fit model” was obtained for each source. We applied the “best-fit model” to the observed spectra, obtaining the unfolded spectra in physical units ( $\text{keV cm}^{-2} \text{s}^{-1} \text{keV}^{-1}$ ) (**eufspec** command in XSPEC). The unfolded spectra are free of instrumental effects.

We next corrected the unfolded spectra for absorption, and shifted them to their rest frame by simply increasing the energies by a factor of  $(1 + z)$ . The redshifted spectra are normalized by dividing the spectra by their corresponding 2–5 keV rest-frame flux, in order to ensure that each spectrum contributes with the same weight to the averaged spectrum. Considering that redshifts of these kinds of sources are different, thus their rest frame spectra have different energy boundaries. Before averaging the spectra, we chose a common energy grid: a bin width of 0.25 keV for energies lower than 8 keV and a bin width of 2 keV above. Then the normalized spectra (flux density values) were redistributed into the new energy bins using formulae (1) and (2) of Corral et al. (2008).

After obtaining the rescaled and rebinned spectra in the rest frame, we averaged them using an un-weighted standard mean. Errors are calculated using formula (3) of Corral et al. (2008).

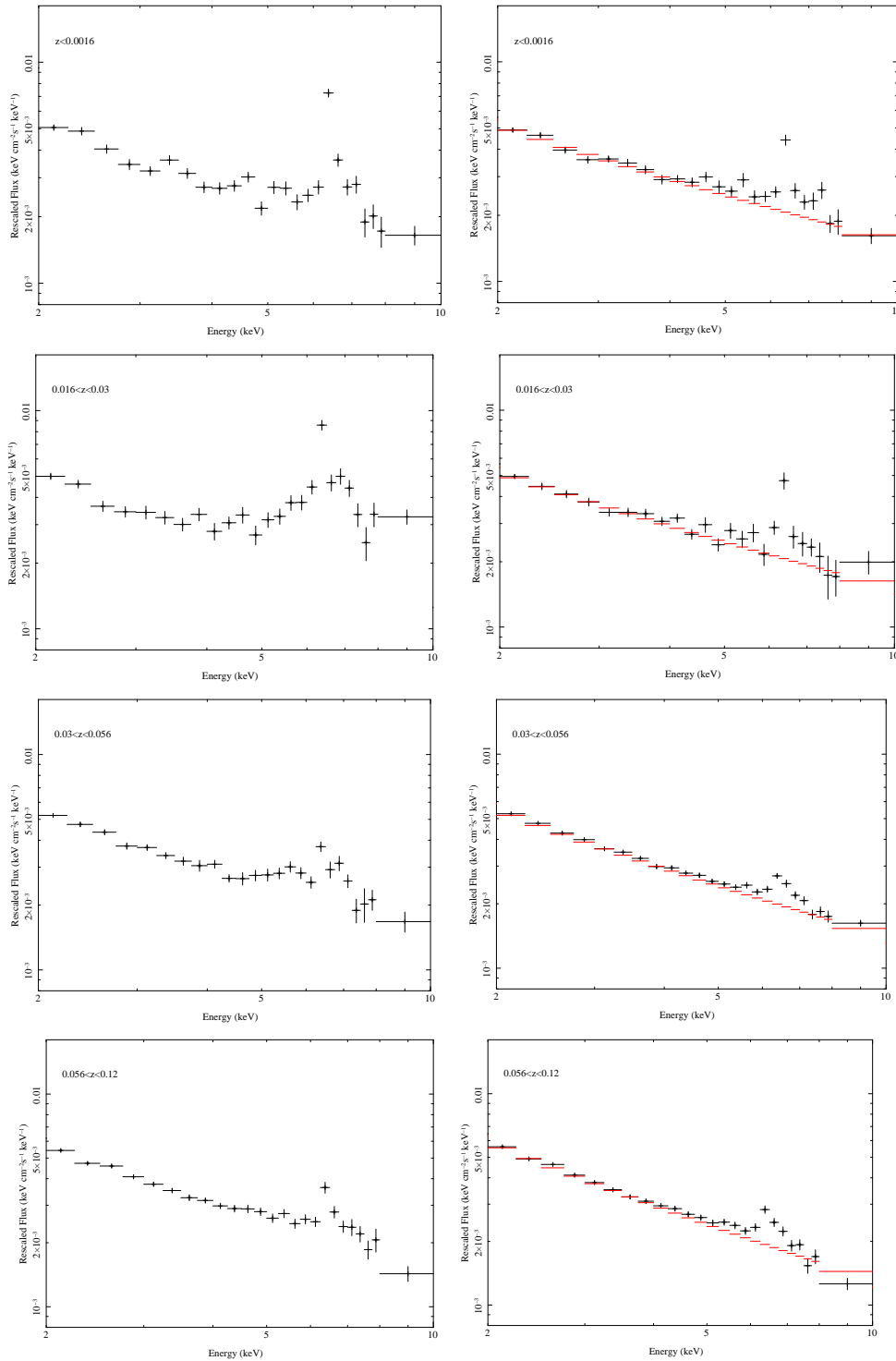


**Fig. 1** Average spectrum for the seven groups. *Left panel*: all AGNs. *Right panel*: type I AGNs.

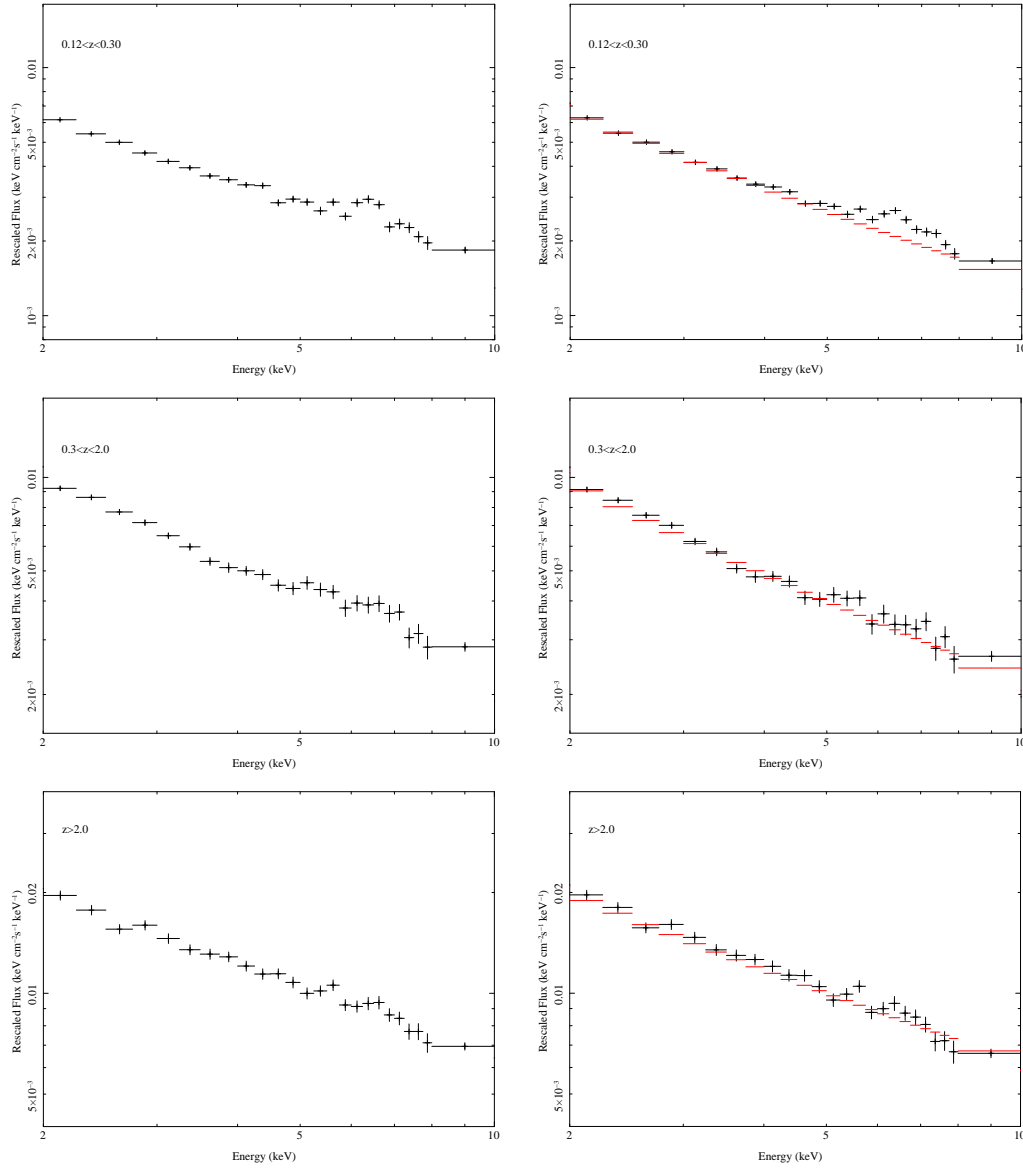


**Fig. 1** *Continued.*

### 3.2 Averaged Spectra

Figure 1 (left panel) shows the resulting averaged spectra. We can see that the averaged spectra for all redshift bins, except the largest two, show prominent line features around 6.4 keV. This indicates that the Fe  $K\alpha$  line should be a common feature among nearby AGNs. Spectra for the two largest redshift bins do not show these line features. This result could be caused because the number of counts collected for the long distance AGN X-ray spectra is not large enough to reach the minimum number of counts necessary to model the continuum and detect a line (Guainazzi et al. 2006). An alternative possibility is that these sources have extreme relativistic blurring which broadens and weakens the line and makes it undetectable (Fabian & Miniutti 2005).

**Table 3** Two Gaussian Fitting Parameters

$z$ -bin	$\chi^2/\text{dof}$	Narrow Gaussian			Broad Gaussian		
		Line energy (keV)	$\sigma$ (eV)	EW (eV)	Line energy (keV)	$\sigma$ (keV)	EW (eV)
0.12–0.3	0.93	6.38±0.12	170±70	50±30	6.73±0.24	1.10±0.25	450±130
0.056–0.12	0.85	6.49±0.06	200±180	200±190	6.25±0.32	1.07±0.35	290±140
0.03–0.056	0.70	6.49±0.07	200±170	140±130	6.40±0.27	1.01±0.35	250±130
0.016–0.03	1.10	6.36±0.09	120±50	340±170	6.67±0.48	0.97±0.52	470±350
<0.116	0.95	6.40±0.09	110±50	280±150	6.41±0.34	1.06±0.46	430±250

Notes:  $\sigma$  represents line width (in keV). EW represents the equivalent width of the line.

However, our present sample includes some type II objects. For these objects, especially for the Compton-thick objects, the spectra may be dominated by a reflection component. In this case, the spectra may show apparent broad residuals but not a broad Fe  $K\alpha$  line. We next excluded these type II objects from our sample and the resulting averaged spectra of type I AGNs are shown in Figure 1 (right panel).

In order to construct the underlying continuum against which we could properly measure the line properties, we applied the same averaging method for the real data to the “best-fit model” obtained from fitting the individual observed spectra. The averaged “best-fit model” spectra, which are used to represent the actual underlying continuum below the emission line, are shown in Figure 1 (right panel, dashed lines). Then we calculated the ratio of the averaged spectra to the underlying continuum. Figure 2 shows the results.

### 3.3 Phenomenological Analysis of the Fe Profile

We fit the Fe profile by two Gaussian components, which represent the narrow and broad Fe lines respectively, so as to get the line width ( $\sigma$ ) and equivalent width (EW). All parameters of the narrow Gaussian are free parameters in our fitting. The central energy and  $\sigma$  of the broad Gaussian, also free parameters, are constrained to be 6–7 keV and  $< 2$  keV respectively. Except for those of the largest two redshift bins, the Fe profiles can be fitted well. The results are tabulated in Table 3 and shown in Figure 2. For the narrow Gaussian component, the line is centered around 6.4 keV and the  $\sigma$  is below 200 eV. Among the five redshift bins, EW values are distributed from  $50 \pm 30$  to  $340 \pm 170$  keV, with a mean of 200 eV. For the broad Gaussian component, the central energy seems a little larger than that of the narrow line and the  $\sigma$  is about 1.0 keV. The EW values of the broad component are distributed from  $250 \pm 130$  to  $470 \pm 350$  eV, with a mean of 380 eV.

The  $\sigma$  and EW of the averaged spectra in each redshift bin are shown in Figure 3. The left panel is for the narrow Fe line, and the right panel is for the broad one. We did not detect any significant variations in the Fe line (neither narrow nor broad Fe component)  $\sigma$  or EW in the redshift range  $z < 0.3$ .

### 3.4 Physical Models

The two-Gaussian fit of the Fe profile in Section 3.3 does not take account of the reflection continuum, and also shows no statistical significance of the broad line. In this section, we will fit the averaged spectra using a series of realistic, physical models, so as to constrain the relativistic broad Fe line better.

We excluded energies below 2 and above 10 keV. For each redshift bin, we first fit the averaged spectra with a power-law (PL) plus a narrow Gaussian line (Gaus). All parameters were free parameters but the line width was constrained to be  $< 200$  eV. Using the “PL+Gaus” model, we obtained

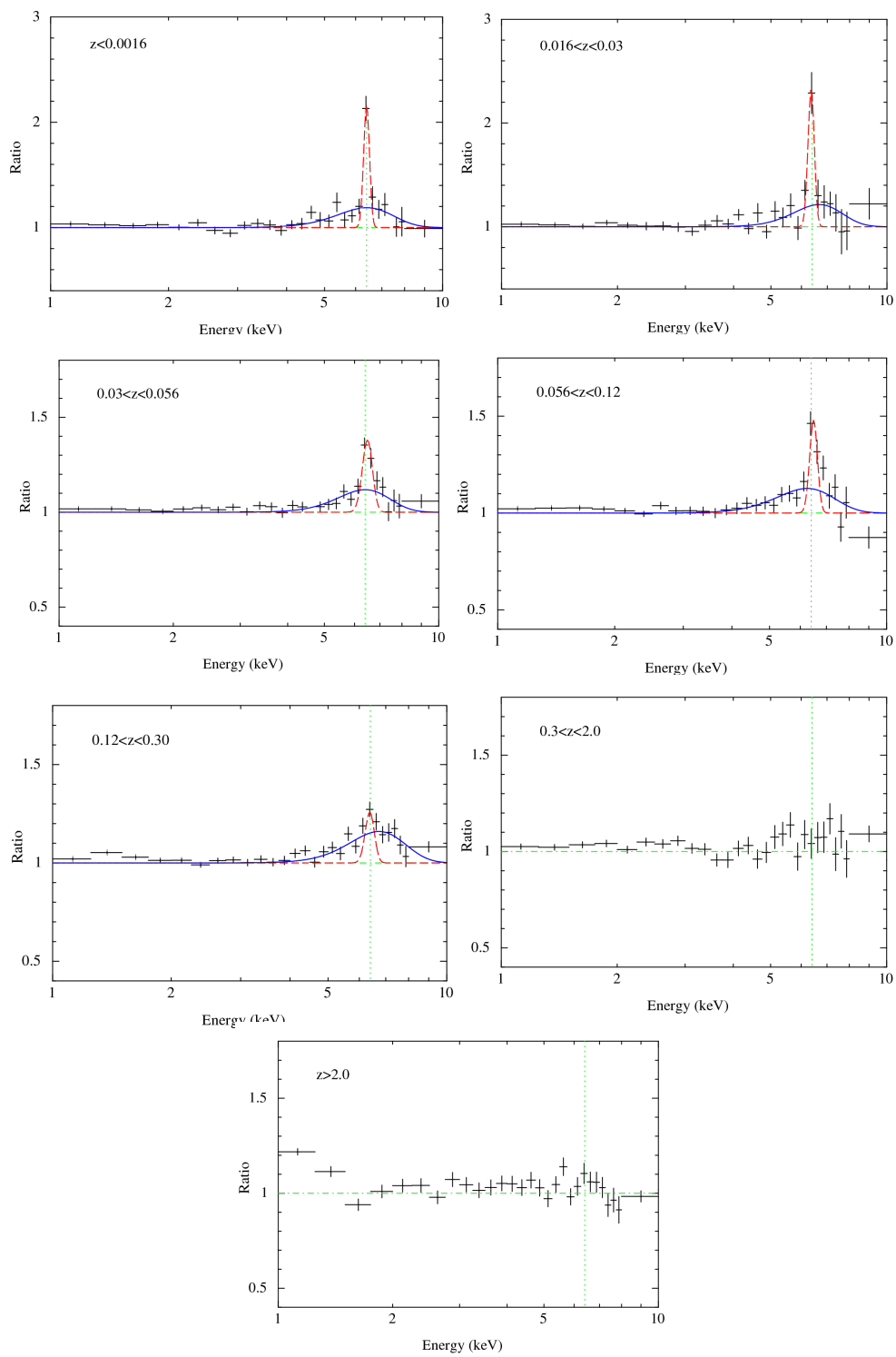


**Fig. 2** Fe line profiles for the seven groups (type I AGNs). The vertical dotted line is at 6.4 keV.

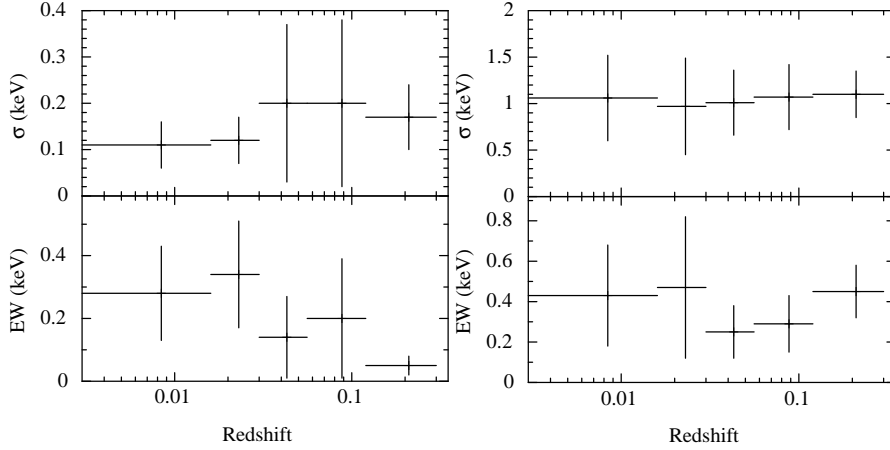


**Fig. 3** Dependence of the Fe line ( $\sigma$ ) width and EW on redshifts. *Left panel*: narrow Gaussian component. *Right panel*: broad Gaussian component.

acceptable fits for the two redshift bins  $0.016 < z < 0.03$  ( $21.87/20 \chi^2/\text{dof}$ ) and  $0.03 < z < 0.056$  ( $25.66/20 \chi^2/\text{dof}$ ), but poor fits for the other three. The fitting results are shown in Table 4. Note that the narrow line was detected at an  $a > 3\sigma$  significance level for all the five redshift bins.

Next, we added a relativistic broad line (laor model, Laor 1991). We found the fits to be relatively insensitive to the emissivity index ( $\beta$ ), with inner and outer radii ( $R_{\text{in}}$ ,  $R_{\text{out}}$ ), which were therefore fixed at  $\beta = 3$ ,  $R_{\text{in}} = 1.235R_g$ , and  $R_{\text{out}} = 400R_g$ . Leaving the Laor line energy ( $E_{\text{laor}}$ ) and inclination angle ( $i$ ) free significantly improved the fits but resulted in unreasonable values (e.g.  $i > 80^\circ$ ,  $E_{\text{laor}} < 6.4$  or  $> 6.9$  keV). We therefore fixed the line energy and inclination angle to 6.4 keV and  $30^\circ$  respectively. In this way, the “PL+Gaus+laor” model and the “PL+Gaus” model yield similar reduced  $\chi^2$ . We then attempted to free one of the two parameters, which can significantly improve the fits.

To provide a more physical realistic description of the data, the “pexrav+Gaus” model was also examined, in which a reflected component was considered (pexrav model, Magdziarz & Zdziarski 1995). The reflector was assumed to have solar elemental abundances. We fixed the cutoff energy to be 100 keV and the inclination angle to be  $30^\circ$ , since our fits were insensitive to them. Using the “pexrav+Gaus” model, we obtained better fits than using the “PL+Gaus” one. The reduced  $\chi^2$  values are significantly improved, especially for the bin  $0.03 < z < 0.056$  ( $25.66/20 \chi^2/\text{dof}$  to  $8.08/19 \chi^2/\text{dof}$ ). The EWs of narrow Fe lines are 70 – 290 eV. Note that the strength of the narrow line and the reflection component are self-consistent (considering the large errors of EW and reflection factor ( $F_{\text{ref}}$ )). According to George & Fabian (1991), in the circumstances of a neutral reflector with solar elemental abundances, assuming  $F_{\text{ref}} = 1$  and inclination angle  $\sim 30^\circ$ , and considering the value of power-law photon index  $\sim 1.8 - 2.0$  obtained from our fits, the predicted EW is 130 – 145 eV.

We also added a laor component to the “pexrav+Gaus” model and applied the same fitting process as for the “PL+Gaus+laor” one. For the three redshift bins  $z < 0.116$ ,  $0.056 < z < 0.12$  and  $0.12 < z < 0.3$ , adding the laor line improved the fits ( $\Delta\chi^2 = 9.07, 11.04$ , and  $10.08$  respectively for two additional parameters), and the EWs of the laor line are  $839_{-601}^{+352}$ ,  $461_{-274}^{+318}$ , and  $308_{-203}^{+178}$  respectively. However, for the other two redshift bins, adding this component did not improve the fits, but rather worsened them, meaning that the broad Fe line was not detected in these two redshift bins. In addition, the EW values of the narrow Fe line were distributed in the range 58 – 290 eV, with a mean 160 eV.

**Table 4** Results of Model Fitting to the Spectra

$z$ -bin	Model	$E_{\text{Gaus}}$ (keV)	$\sigma_{\text{Gaus}}$ (eV)	$EW_{\text{Gaus}}$ (eV)	$F_{\text{ref}}$	$E_{\text{laor}}$ (keV)	$EW_{\text{laor}}$ (eV)	Inc angle ( $^{\circ}$ )	$\chi^2/\text{dof}$
0.12-0.3	PL+Gaus	$6.39^{+0.05}_{-0.05}$	$200^p$	$103^{+38}_{-37}$					29.14/19
	PL+Gaus+laor	$6.36^{+0.06}_{-0.06}$	$200^{+56}_{-40}$	$80^{+50}_{-48}$		$7.22^{+0.09}_{-0.11}$	$320^{+179}_{-201}$	$30^f$	17.03/17
		$6.36^{+0.07}_{-0.08}$	$169^{+75}_{-42}$	$52^{+51}_{-49}$		$6.40^f$	$423^{+343}_{-240}$	$89.15^{+p}_{-1.53}$	14.89/17
	pexrav+Gaus	$6.36^{+0.06}_{-0.07}$	$200^{+p}_{-55}$	$72^{+92}_{-45}$	$1.46^{+0.50}_{-0.54}$				23.58/18
	pexrav+Gaus+laor	$6.35^{+0.07}_{-0.07}$	$177^{+p}_{-78}$	$58^{+44}_{-43}$	$1.04^{+0.57}_{-0.56}$	$6.99^{+0.63}_{-0.34}$	$304^{+191}_{-212}$	$40.71^{+43.03}_{-11.94}$	13.24/15
		$6.35^{+0.07}_{-0.06}$	$168^{+56}_{-39}$	$58^{+47}_{-46}$	$1.02^{+0.40}_{-0.43}$	$6.40^f$	$308^{+178}_{-203}$	$57.24^{+2.56}_{-2.18}$	13.50/16 $\checkmark$
0.056-0.12	PL+Gaus	$6.45^{+0.03}_{-0.03}$	$200^p$	$223^{+58}_{-55}$					34.07/20
	PL+Gaus+laor	$6.42^{+0.03}_{-0.04}$	$152^{+47}_{-28}$	$133^{+65}_{-61}$		$7.07^{+0.07}_{-0.06}$	$526^{+289}_{-217}$	$30^f$	14.52/18
		$6.42^{+0.03}_{-0.04}$	$147^{+48}_{-26}$	$132^{+61}_{-59}$		$6.40^f$	$530^{+253}_{-225}$	$52.34^{+1.72}_{-1.58}$	15.18/18
	pexrav+Gaus	$6.43^{+0.04}_{-0.04}$	$160^{+p}_{-32}$	$141^{+67}_{-64}$	$2.30^{+0.67}_{-0.70}$				26.59/19
	pexrav+Gaus+laor	$6.42^{+0.03}_{-0.04}$	$145^{+39}_{-30}$	$124^{+62}_{-62}$	$0.63^{+0.72}_{-p}$	$7.09^{+0.09}_{-0.06}$	$468^{+346}_{-269}$	$30^f$	14.56/17
		$6.42^{+0.03}_{-0.04}$	$143^{+38}_{-29}$	$124^{+60}_{-58}$	$0.68^{+0.70}_{-0.65}$	$6.40^f$	$461^{+318}_{-274}$	$52.92^{+2.17}_{-1.66}$	15.15/17 $\checkmark$
0.03-0.056	PL+Gaus	$6.47^{+0.03}_{-0.03}$	$200^p$	$173^{+47}_{-44}$					25.66/20
	PL+Gaus+laor	$6.44^{+0.02}_{-0.04}$	$169^{+p}_{-25}$	$119^{+56}_{-53}$		$6.91^{+0.10}_{-0.10}$	$259^{+179}_{-178}$	$30^f$	19.02/18
		$6.45^{+0.04}_{-0.04}$	$155^{+p}_{-29}$	$102^{+58}_{-51}$		$6.40^f$	$489^{+355}_{-242}$	$87.78^{+2.00}_{-0.75}$	12.03/18
	pexrav+Gaus	$6.45^{+0.03}_{-0.04}$	$145^{+40}_{-33}$	$94^{+52}_{-49}$	$2.57^{+0.48}_{-0.50}$				8.08/19 $\checkmark$
	pexrav+Gaus+laor	$6.44^{+0.03}_{-0.04}$	$145^{+51}_{-97}$	$94^{+53}_{-52}$	$2.33^{+0.48}_{-0.69}$	$7.94^{+0.91}_{-0.47}$	$167^{+363}_{-167}$	$30^f$	6.73/17
		$6.44^{+0.04}_{-0.04}$	$142^{+40}_{-34}$	$92^{+51}_{-49}$	$2.36^{+0.58}_{-0.53}$	$6.40^f$	$135^{+221}_{-135}$	$62.65^{+p}_{-7.12}$	6.82/17
0.016-0.03	PL+Gaus	$6.36^{+0.03}_{-0.03}$	$121^{+22}_{-21}$	$410^{+136}_{-129}$					21.87/20
	PL+Gaus+laor	$6.35^{+0.03}_{-0.09}$	$105^{+23}_{-76}$	$330^{+146}_{-140}$		$7.04^{+0.23}_{-0.21}$	$442^{+577}_{-407}$	$30^f$	17.48/18
		$6.35^{+0.03}_{-0.09}$	$106^{+23}_{-76}$	$333^{+144}_{-145}$		$6.40^f$	$442^{+573}_{-400}$	$52.29^{+4.98}_{-5.77}$	17.51/18
	pexrav+Gaus	$6.35^{+0.03}_{-0.11}$	$94^{+26}_{-73}$	$290^{+126}_{-125}$	$3.86^{+2.10}_{-1.60}$				15.36/19 $\checkmark$
	pexrav+Gaus+laor	$6.34^{+0.04}_{-0.08}$	$87^{+30}_{-72}$	$274^{+158}_{-131}$	$6.93^{+3.39}_{-2.76}$	$4.04^{+0.09}_{-0.09}$	$126^{+134}_{-126}$	$30^f$	12.24/17
		$6.35^{+0.04}_{-0.11}$	$93^{+29}_{-72}$	$287^{+130}_{-139}$	$2.98^{+2.50}_{-1.72}$	$6.40^f$	$161^{+649}_{-161}$	$53.26^{+p}_{-p}$	14.95/17
<0.116	PL+Gaus	$6.39^{+0.02}_{-0.02}$	$106^{+14}_{-15}$	$317^{+84}_{-83}$					31.72/20
	PL+Gaus+laor	$6.38^{+0.06}_{-0.04}$	$84^{+16}_{-15}$	$237^{+93}_{-83}$		$7.17^{+0.06}_{-0.07}$	$896^{+368}_{-548}$	$30^f$	16.80/18
		$6.38^{+0.03}_{-0.03}$	$85^{+15}_{-22}$	$241^{+88}_{-86}$		$6.40^f$	$889^{+350}_{-563}$	$55.17^{+1.33}_{-2.07}$	17.27/18
	pexrav+Gaus	$6.39^{+0.05}_{-0.03}$	$85^{+16}_{-43}$	$244^{+86}_{-88}$	$2.80^{+1.44}_{-1.14}$				26.22/19
	pexrav+Gaus+laor	$6.38^{+0.09}_{-0.07}$	$80^{+21}_{-80}$	$227^{+94}_{-90}$	$0.62^{+1.27}_{-0.62}$	$6.93^{+0.64}_{-1.06}$	$859^{+499}_{-598}$	$39.94^{+30.17}_{-23.69}$	16.63/16
		$6.38^{+0.09}_{-0.09}$	$81^{+17}_{-55}$	$230^{+83}_{-89}$	$0.61^{+1.13}_{-0.61}$	$6.40^f$	$839^{+352}_{-601}$	$53.34^{+1.45}_{-1.80}$	17.15/17 $\checkmark$

Notes:  $\sigma$  represents line width (in eV); EW represents the equivalent width of the line;  $F_{\text{ref}}$  represents the reflection factor; Inc angle represents inclination angle. The superscripted  $p$  fit parameter denotes being pegged at the hard limit; The superscripted  $f$  denotes a fixed parameter;  $\checkmark$  means the fitting is the best one in terms of being physical and reasonable.

#### 4 SUMMARY

With data from the EPIC-pn detectors, we used a sample of 381 AGNs (271 type I) with redshift identifications. We analyzed the spectra of individual objects and used an averaging technique to stack spectra of the different redshifted AGNs. We found that the stacked rest frame spectra of the present sample showed an Fe K $\alpha$  component in the redshift range  $z < 0.3$ .

Phenomenological analysis of the Fe profile suggests that the  $\sigma$  of the Fe line does not show significant dependence on redshift in the redshift range  $z < 0.3$ , meaning that the spins of SMBHs do not show significant cosmic evolution at low redshift ( $z < 0.3$ ). This is consistent with the result of Wang et al. (2009). However, they find that the spins of SMBHs in a quasar population strongly evolve at high redshift: black holes at  $z \sim 1 - 2$  are spinning much faster.

The “pexrav+gau+laor” model provided the best (in a  $\chi^2$  sense) and most physically self-consistent explanation. In this model, we significantly detected a narrow Fe line at 6.4 keV with  $\sigma \sim 130$  eV,  $EW \sim 160$  eV, corresponding to the Fe  $K\alpha$  emission line emitted from neutral or weakly-ionized material (e.g., the dust torus far from the central SMBH). Previous observations have shown that the narrow Fe  $K\alpha$  line is almost a ubiquitous characteristic in local AGN X-ray spectra (Page et al. 2004). Our work confirms this result. We also detect a broad line component in three redshift bins ( $z < 0.116$ ,  $0.056 < z < 0.12$  and  $0.12 < z < 0.3$ ). The EWs of the broad lines are  $839^{+352}_{-601}$ ,  $461^{+318}_{-274}$ , and  $308^{+178}_{-203}$  eV respectively, and the mean is  $\sim 522$  eV with a large standard deviation. This means a broad Fe line is not ubiquitous.

Another result from our work is that there is not any change in EW of the Fe line with the redshift in redshift range  $z < 0.3$ . Brusa et al. (2005) studied the Fe line of 352 AGNs detected in the *Chandra* Deep Field North and South. They also found that the average rest-frame EW of the Fe line does not show significant changes with redshift. They regard the lack of any dependence of the line intensity on redshift as a constant iron abundance with redshift (Brusa et al. 2005).

We would like to point out that the present method of averaging unfolded spectra is limited to some degree by its dependence on the spectral model applied. Another limitation is assuming that the averaged “best-fit model” spectra represent the actual underlying continuum below the emission line. This assumption may cause some uncertainty. Corral et al. (2008) simulated the underlying continuum, and claimed that the simulated continuum shows broad residuals at 5–10 keV which was an obstacle to fitting the Fe  $K\alpha$  line, especially the broad Fe  $K\alpha$  line. We expect that future X-ray missions with much larger effective collecting areas at 6 keV will detect more photons with higher spectral resolutions and give more robust results regarding the cosmic evolution of the Fe line profiles.

**Acknowledgements** We are grateful to Dr. Qu Jin-Lu for help in reduction of X-ray data. We appreciate the discussions among the members of the IHEP AGN group. We thank the anonymous referee for helpful comments. This research has made use of the NASA/IPAC Extra-galactic Database (NED) which is operated by the Jet Propulsion Laboratory, California Institute of Technology, under contract with the National Aeronautics and Space Administration. This work was funded by the National Natural Science Foundation of China (NSFC; Grant No. 10821061) and by the National Basic Research Program of China (973 program; Nos. 2007CB815103 and 2009CB824800).

## References

- Arnaud, K. A. 1996, in ASP Conf. Ser. 101, 17  
 Brusa, M., Gilli, R., & Comastri, A. 2005, ApJ, 621, L5  
 Corral, A., Page, M. J., Carrera, F. G., et al. 2008, A&A, 492, 71  
 Fabian, A. C., Rees, M. J., Stella, L., et al. 1989, MNRAS, 238, 729  
 Fabian, A. C., Vaughan, S., Nandra, K., et al. 2002, MNRAS, 335, 1  
 Fabian, A. C., & Miniutti, G. 2005, arXiv:astro-ph/0507409  
 George, I. M., & Fabian, A. C. 1991, MNRAS, 249, 352  
 Guainazzi, M., Bianchi, S., & Dovciak, M. 2006, AN, 327, 1032  
 Laor, A. 1991, ApJ, 376, 90  
 Magdziarz, P., & Zdziarski, A. A. 1995, MNRAS, 273, 837  
 Nandra, K., George, I. M., Mushotzky, R. F., Turner, T. J., & Yaqoob, T. 1997, ApJ, 477, 602  
 Nandra, K., O’Neill, P. M., George, I. M., et al. 2007, MNRAS, 382, 194  
 Page, K. L., O’Brien, P. T., Reeves, J. N., et al. 2004, MNRAS, 347, 316  
 Streblyanska, A., Hasinger, G., Finoguenov, A., et al. 2005, A&A, 432, 395  
 Tanaka, Y., Nandra, K., Fabian, A. C., et al. 1995, Nature, 375, 659  
 Wang, J.-M., Hu, C., Li, Y.-R., et al. 2009, ApJ, 697, L141  
 Yaqoob, T., & Padmanabhan, U. 2004, ApJ, 604, 63